Photoelectron angular distributions in photodetachment from polarized d-like states: The case of HO_2^-

Christopher C. Blackstone, Adam A. Wallace, and Andrei Sanov *

Department of Chemistry and Biochemistry, The University of Arizona, Tucson, AZ 85721, U.S.A.

* Email, sanov@arizona.edu

We present a photoelectron imaging study of the angular distributions in HO₂⁻ photodetachment. The transitions studied correspond to electron detachment from the a" HOMO and a' HOMO-1 of HO₂-, yielding the neutral hydroperoxy radical in the ground and first excited electronic states. The experimental results are analysed using the p-d variant of the general model for photodetachment from mixed-character states. In this model, the parent anion molecular orbitals or the corresponding Dyson orbitals are described as superpositions of atomic p and dfunctions placed at a chosen centre in the molecular frame. As photoelectron angular distributions are sensitive to the long-range scaling of the parent orbitals, modelling the experimental results yields insight into the long-range behaviour of the anionic wavefunctions. In the model, the long-range behaviour of diffuse orbitals is parameterized using the effective charges defining the basis functions. These charge parameters do not correspond to any physical charges in the anion, but describe the long-range scaling of the p and d components of the model function and, therefore, the parent anion orbital. The experimental and model results for HO₂⁻ are compared to NO⁻ and O₂⁻, shedding light on the effects of molecular symmetry and chemical bonding structures on the photoelectron angular distributions.

Keywords: negative ions; photoelectron angular distributions; mixed-character states; hydroperoxide anion; hydroperoxy radical

1. Introduction

The hydroperoxy radical HO₂ is ubiquitous in the Earth atmosphere, where it participates in a myriad of reactions involved in natural and pollutant-driven chemistry [1-13]. The corresponding hydroperoxide anion HO₂⁻ is an important intermediate in the solution-phase consumption of ozone, among other reactions [14,15]. Despite their clear and broad relevance, as well as the extensive studies conducted on these seemingly simple triatomic species, their chemistry is not yet fully understood.

In the atmosphere, the hydroperoxy radical is formed primarily through the reaction of carbon monoxide with hydroxyl radicals, photolysis of carbonyls, and oxidation of volatile organic compounds (VOCs) [2]. It further engages in an array of important atmospheric cycles, including the production of secondary organic aerosols (SOAs) and tropospheric ozone, which have adverse impacts on public health, and the formation of OH radicals, which drive the oxidative capacity of the atmosphere [1,2,5]. The latter means that HO2 itself is a major driver of this capacity, and the details of its chemistry are essential to understanding the atmosphere's complex network of reactions. Consequently, there is significant recent work on developing new methods for detecting and measuring its presence in the atmosphere, as well as understanding its chemistry, in order to produce accurate models of its behaviour [2,16-18].

The hydroperoxide anion is readily produced through the deprotonation of hydrogen peroxide. This anion drives the solution-phase decomposition of ozone and production of OH radicals through the peroxone process, used, incidentally, as a means of disinfecting drinking water [14,15]. This chemistry and its application to new industrial processes were the subject of recent investigations [14,15]. Analogous processes may be possible in the atmosphere, as well, though their direct evidence is less abundant. Direct investigations of the hydroperoxide anion in the gas phase are

therefore of crucial interest to understanding its chemistry in the atmosphere.

The photoelectron spectrum of HO₂⁻ has been studied previously [19,20]. In the most recent work, Clifford et al. observed two electronic states of the neutral radical, each displaying a single vibrational progression [19]. The adiabatic electron affinity (EA) of HO₂ was determined to be 1.089(6) eV, with a splitting between the ground and excited states of 0.871(7) eV, placing the onset of the excited state at 1.960 eV. The vibrational progression in each state corresponded to the O–O stretching mode, with a frequency of 1097.63 cm⁻¹ in the ground state and 929.068 cm⁻¹ in the excited state [19]. These values were in excellent agreement with previous work on the system [20-23], including the photoelectron spectrum collected by Oakes et al. [20], who found the EA to be 1.078(17) eV, as well as the near-IR emission measurement of Tuckett et al. [22], who found the ground-to-excited state splitting to be 7029.48(10) cm⁻¹.

In this work, we investigate on the photoelectron angular distributions (PADs) in HO₂⁻ photodetachment and focus on what they reveal about the electronic structure and the photodetachment process. We also compare HO₂⁻ to O₂⁻ and NO⁻, to explore the role of molecular symmetry in the context of quantitative modelling of PADs. The HO₂⁻ PADs have not been studied in any detail to this point. Since the photoelectron spectrum, on the other hand, has been well-characterized, it allows us to unambiguously separate the PADs in the photodetachment transitions to the ground and excited states of the HO₂ radical, facilitating the necessary analysis. Although many of the electronic-structure and photodetachment details presented here will be looked at primarily from the physics point of view, it is these physics that ultimately control the environmental chemistry of this important anion and the corresponding neutral radical.

Photoelectron angular distributions have attracted a lot of attention, particularly since the introduction of Eppink and Parker's revolutionary velocity-map approach

[24,25] to photoelectron imaging [26,27]. On the theory side, since the dawn of the field, the analysis of the experimental PADs used to rely heavily on the Cooper-Zare central-potential formula [28-30], rooted in the earlier derivations by Bethe [31]. Its widespread practical application had been facilitated by Hanstorp et al.'s breakthrough idea [32] to use Wigner's theory [33] to approximate the relative scaling of the partial-wave transition matrix elements appearing in the Cooper-Zare formula. Although the Cooper-Zare formula is strictly valid only for atomic systems, there have been successful attempts to overcome this limitation in describing molecular anions using the same central-potential approach. A famous example is the modelling of O_2 - photodetachment as electron emission from a "d-like" orbital [34-37], which is indeed a good approximation of the π_g^* HOMO (highest-occupied molecular orbital) of O_2 -.

However, O_2^- is an exception rather than the rule. The orbitals of most molecular systems cannot be assigned a single "effective" value of the orbital angular momentum quantum number (l), which is the defining parameter in the Cooper-Zare formula. For example, photodetachment from sp^n hybrid orbitals, which are ubiquitous in organic compounds, cannot be modelled within the central-potential formalism. Neither l=0 (for s) nor l=1 (for p) are acceptable descriptions of a hybrid, and one certainly cannot use the $\langle l \rangle = n/(n+1)$ weighted-average, because such intermediate fractional quantities are forbidden by quantum mechanics. A different approach was needed and developed, initially for mixed s-p character molecular orbitals (MO) [38-40]. It was later generalized for states of any mixed character [41], whereas the parent MO, from which the electron originates, is described as a superposition of atomic-like functions all placed at the same centre in the molecular frame.

In using such superpositions, the model approach has some similarity to the Linear Combination of Atomic Orbitals MO theory (LCAO-MO), but differs from it in

that the mixed-character basis functions are all located at the same centre. In this regard, the model functions are similar to hybrid atomic orbitals, but differ from them too, in that the expansion centre does not have to correspond to any atom in the system. For example, adopting the model language to superoxide, the dominant contribution to the model function describing the π_g^* HOMO of O_2^- is a d function centred at the middle of the O–O bond. This function does not correspond to any stationary orbitals of either of the two O atoms, but nonetheless makes it possible to analyse the O_2^- PADs using the Cooper-Zare formula with an effective value of l = 2 [34-37,42].

While the O_2^- case involves just one dominant l component of the HOMO, in most other systems more expansion terms are necessary. Formally speaking, the atomic-like functions located on an arbitrary centre comprise a complete basis set, and therefore the expansion is rigorously justified in every case. Once the expansion is defined, the outgoing electron is described as a superposition of partial waves with orbital angular momentum quantum numbers l_f , related to the corresponding quantum numbers of the basis functions by the $l_f = l \pm 1$ selection rule. The key to successful application of the mixed-character model is limiting the number of the terms to a few carefully chosen and properly placed basis functions, capturing the significant properties of the MO without obscuring the conceptual insight from the analysis with a myriad of expansion coefficients and other adjustable parameters.

In this work, we adopt the p-d variant of the general mixing model [41] to describe the PADs in the photodetachment from the HOMO and HOMO-1 of HO₂⁻, in comparison to the HOMOs of NO⁻ and O₂⁻. The photodetachment orbitals in the first two systems are well described as distorted (polarized) d-like orbitals, while the O₂⁻ HOMO serves as an unpolarized d-like reference case. The p-d mixing approach works well in these systems, because the MOs involved can be adequately approximated by

mixed-character *p-d* functions, generally defined as:

$$|\phi_{pd}\rangle = \sqrt{1 - \gamma_d}|p\rangle + \sqrt{\gamma_d}|d\rangle,$$
 (1)

where γ_d is the fractional d-character ($0 \le \gamma_d \le 1$). Any relative phase factors between the p and d components of Eq. (1) are absorbed into the kets. This expression is well suited for the description of lopsided d-like MOs, as illustrated in Figure 1. Specifically, using the molecular-frame (MF) coordinate definitions included in the figure, superposition of the real $3d_{zx}$ ($|d\rangle$ in the figure) and $2p_x$ ($|p\rangle$) orbitals placed at the same centre in the MF yields a lopsided d-like model function, resembling π^* orbitals in many diatomic and pseudo-diatomic systems, such as NO⁻ and HO2⁻. Conveniently, Eq. (1) with $\gamma_d = 1$ also describes the π_g^* MOs of homonuclear diatomics, such as O2⁻, allowing for direct comparison of a wide array of systems analysed using the same formalism.

The mixed-character model can be applied using either canonical Hartree-Fock (HF) or Dyson orbitals. Dyson orbitals take into account electron correlation and relaxation effects in many-electron systems [43-45] and are, therefore, rigorously more appropriate for describing photodetachment transitions [46]. However, canonical HF orbitals often provide a good (enough) approximation, hold the appeal of reduced computational complexity, while also allowing a more direct insight into the electronic wavefunction of the anion itself, rather than its overlap with the final state of the transition. Previous experimentation with both HF and Dyson orbitals indicated only small differences in the results of the *s-p* variant of the mixed-character model [37,39]. In this work we compare the performance of both types of orbitals in the *p-d* mixing context.

In the next section, we outline our experimental approach to HO_2^- photodetachment. The results are presented in section 3. In section 4, we summarize the p-d mixing formalism and the details of modelling the PADs from the p-d-like HOMO and

HOMO–1 of HO₂⁻, in comparison to NO⁻ and O₂⁻. The O₂⁻, NO⁻, and HO₂⁻ series is used to spotlight the effects of gradually diminishing molecular symmetry on the PADs from (distorted) *d*-like MOs. Section 5 presents an overall discussion, while Section 6 summarizes the overarching conclusions.

2. Experimental methods

The experiments were carried out using the negative-ion [47] spectrometer described in detail elsewhere [48,49]. Hydroperoxide anions were produced through the oxidation of methoxide anions CH₃O⁻ in an electron-impact ionized supersonic expansion. A methanol precursor was seeded in oxygen carrier gas and deprotonated in the expansion by O⁻ formed by electron-bombardment of O₂. The resulting methoxide anions then reacted with O₂ to form HO₂⁻, according to the known chemistry [50,51]:

$$CH_3O^- + O_2 \to CH_2O + HO_2^-.$$
 (2)

The resulting anions were separated according to their masses in the Wiley-McLaren time-of-flight mass-spectrometer [52] and intersected with a pulsed laser beam in the detection region of the instrument. Photoelectron images of HO₂⁻ were collected at eight wavelengths: 306, 355, 406, 607, 612, 622, 797, and 812 nm. The 355 nm light was produced as the third harmonic of a Nd:YAG laser (Spectra Physics; 5 mJ/pulse, ~6 ns pulse duration). The 607, 612, and 622 nm light was generated by the fluorescence of Rhodamine 640 dye in an ND6000 dye laser pumped by Surelite II-20 Nd:YAG (Continuum, Inc.). 306 nm was obtained by frequency doubling the 612 nm output. The 797 and 812 nm light was produced using LDS 821 dye in the same dye laser, and 406 nm—by frequency doubling the 812 nm output.

Photoelectron images were collected using a velocity-map [24,25] photoelectron

imaging [26,27] assembly, mapping the photodetached electron in the direction perpendicular to the ion and laser beams [48,49]. The 607, 612, and 622 nm images were collected with the potentials of –330, 0, and +900 V, applied respectively to the bottom, middle, and top plates of the velocity-map imaging (VMI) lens. The 306, 355, 797, and 812 nm images were collected with the respective VMI potentials of –220, 0, and +600 V. At 406 nm, the –165, 0, and +450 V potentials were used. The highest-energy 306 nm images exhibited slight elliptic distortions and were corrected using the circularization tool in the PyAbel program package [53,54].

3. Experimental results

The raw and Abel-transformed [27,55] photoelectron images of HO₂⁻ collected at (a) 306 nm, (b) 355 nm, (c) 406 nm, (d) 607 nm, (e) 612 nm, (f) 622 nm, (g) 797 nm, and (h) 812 nm are presented in the top part of Figure 2. The corresponding photoelectron spectra are all plotted together for easy comparison in the bottom part of the figure (i). The spectra are plotted vs. electron binding energy, eBE $\equiv h\nu$ – eKE, where $h\nu$ is the photon energy and eKE stands for electron kinetic energy.

At 622 nm and shorter wavelengths, two electronic states of neutral HO₂ are accessed, with vibrational progressions within each state resolved either partially or nearly completely. The spectra are consistent with the past work on HO₂⁻ [19-23] and will not be discussed here in detail. According to our spectra, the adiabatic electron affinity of the ground X^2A'' state of the peroxy radical is EA = 1.089(11) eV. The corresponding origin peak is marked in Figure 2(i) with an asterisk. This result compares favourably with the EA values of 1.078(17) eV and 1.089(6) eV from the two previous measurements [19,22]. The onset of the second electronic band, corresponding to the A^2A' excited state of HO₂, whose origin is marked with two asterisks in Figure

2(i), occurs at 1.951(2) eV, compared to the 1.960 eV and 1.950 eV values determined previously [19,20,22]. Also consistent with the previous studies, the ~1100 and 900 cm⁻¹ vibrational progressions, observed within the two electronic bands, correspond to the O–O stretch in the respective neutral states.

Transitions from the anion to both the X^2A'' and A^2A' states of neutral HO₂ exhibit nearly isotropic PADs at low eKE, but become increasingly perpendicular with increasing eKE. This trend can be noted even by visual inspection of the images in Figure 2(a)-(h). The values of the anisotropy parameter β , determined for various vibrational bands, are plotted as a function of $\varepsilon \equiv$ eKE in Figure 3. Figure 3(a) presents the data for the first photodetachment transition, yielding HO₂(X^2A''), while Figure 3(b) shows the corresponding results for the A^2A' excited state.

4. Theoretical modelling

4.1. The p-d variant of the mixed-character model

To analyse the observed trends, we turn to the p-d variant of the general model describing PADs in molecular-anion photodetachment from states of any mixed character. According to the general formalism [41], the dependence of the anisotropy parameter β on eKE (ε) in photodetachment from a p-d orbital defined by Eq. (1) is given by:

$$\beta = \frac{(1 - \gamma_d)B_2\varepsilon(2A_1^2\varepsilon^2 - 4A_1\varepsilon\cos\delta_{2,0}) + \gamma_dA_1^2\varepsilon^2(2 + 12A_2^2\varepsilon^2 - 36A_2\varepsilon\cos\delta_{3,1})/5}{(1 - \gamma_d)B_2\varepsilon(1 + 2A_1^2\varepsilon^2) + \gamma_dA_1^2\varepsilon^2(2 + 3A_2^2\varepsilon^2)}$$
(3)

where A_1 , A_2 , and B_2 are the Hanstorp-style [32] coefficients, describing the relative scaling of the $l \to l_f = l \pm 1$ photodetachment channels. Here, l = 1 for $|p\rangle$ and 2 for $|d\rangle$ in Eq. (1), while l_f is the corresponding quantum number of the free electron ($l_f = 0, 1, 2,$

and 3 for the s, p, d, and f partial waves, respectively). A_1 in Eq. (3) is the coefficient introduced explicitly by Hanstorp et al. [32] to describe the scaling of the $p \rightarrow d$ and $p \rightarrow s$ channels in O^- photodetachment. Here, it describes the relative scaling of the l=1 $\rightarrow l_f=2$ and $l=1 \rightarrow l_f=0$ channels, originating from the p component of the initial state. A_2 is a similar coefficient for the d component of the model function in Eq. (1): $l=2 \rightarrow l_f=3$ relative to $l=2 \rightarrow l_f=1$. B_2 , on the other hand, is a Hanstorp-style coefficient, not defined by Hanstorp himself, but based on the same physical assumptions as the original Hanstorp A coefficients. B_2 and other B coefficients appearing in the mixed-character model arise when the initial state of the electron is a combination of l_i components, as in Eq. (1). B_2 specifically describes the scaling of the $l=1 \rightarrow l_f=2$ photodetachment channel relative to $l=2 \rightarrow l_f=1$ [41].

Equation (3) also includes the phase shifts between the outgoing (d and s) and (f and p) partial waves: $\delta_{2,0} \equiv (\delta_2 - \delta_0)$ and $\delta_{3,1} \equiv (\delta_3 - \delta_1)$. These phase shifts arise due to the interactions between the departing electron and the remaining neutral. They tend to be small, because the final-state electron-neutral interactions themselves are weak. The phase shifts, reflecting the differences in these interactions, are calculated as deltas of small absolute quantities and therefore assured to be small themselves.

Past studies have shown that the typical values of $\cos \delta_{2,0}$ (for the *s-d* phase shift in detachment from *p* orbitals) range between 0.88 and 0.98 [32,35,36,42,56,57]. In this work, we fix $\cos \delta_{2,0}$ at 0.95, a value within this range, allowing the model to capture the physics without introducing an additional free parameter. We similarly fix the *p-f* phase shift at $\cos \delta_{3,1} = 0.95$, as determined in the previous analysis of O_2^- data [57]. Assuming that the phase shifts in HO_2^- , O_2^- , and NO^- are similar, we will use the above cosine values for all three systems.

This leaves four yet undefined parameters in Eq. (3): A_1, A_2, B_2 , and γ_d . As

discussed previously, the Hanstorp coefficients A_1, A_2 , and B_2 depend on the spatial extent of the MO, particularly in the long range [32,37,41]. Recall that in elementary atomic structure the scaling of an orbital at large r is controlled by the effective nuclear charge appearing in the exponent of the radial function. We assume that the $|p\rangle$ and $|d\rangle$ parts of Eq. (1) are represented specifically by the hydrogenic 2p and 3d orbitals, placed at the centre of the O–O bond. The corresponding radial functions

$$R_{2p}(r) = \frac{1}{2\sqrt{6}} \zeta_{2p}^{5/2} r e^{-\zeta_{2p} r/2} \tag{4}$$

$$R_{3d}(r) = \frac{2\sqrt{2}}{81\sqrt{15}} \zeta_{3d}^{7/2} r^2 e^{-\zeta_{3d}r/3}$$
 (5)

are parameterized by the respective charges ζ_{2p} and ζ_{3d} . With the origin of these functions ($\vec{r} = 0$) being at the centre of the O–O bond, ζ_{2p} and ζ_{3d} do not correspond to any physical charges in the molecule. For this reason, they should not be confused with effective nuclear, atomic, Mulliken [58], or Hirshfeld [59] charges. They cannot be evaluated using, for example, the Slater rules [60] or the self-consistent field screening constants [61]. They are but model parameters defining the spatial extents of the basis functions: the smaller the ζ_{2p} and ζ_{3d} , the more diffuse the corresponding functions.

According to the derivation in Ref. [41], given ζ_{2p} and ζ_{3d} , the three Hanstorp coefficients A_1, A_2 , and B_2 can be expressed in terms of just these two parameters:

$$A_1 = \frac{16}{\zeta_{2n}^2}, \qquad A_2 = \frac{144}{5\zeta_{3d}^2}, \qquad B_2 = \frac{2^9 \zeta_{3d}^7}{5 \cdot 3^6 \zeta_{2n}^9} \tag{6}$$

All three coefficients in (6) are given in atomic units (of reciprocal energy). These expressions appeared in Eq. (43) in Ref. [41], but due to a typographical error the B_2 formula there included an incorrect power of ζ_{2p} (2 instead of the correct 9). Given the

parametrization of A_1 , A_2 , and B_2 in terms of ζ_{2p} and ζ_{3d} , the number of parameters in Eq. (3) is reduced to three total: ζ_{2p} , ζ_{3d} , and γ_d . Among these, γ_d can be determined from ab initio calculations, leaving the effective charges ζ_{2p} and ζ_{3d} as the only free model parameters to be deduced from the experimental data.

4.2. Application of the p-d mixing model to HO_2^-

The geometry of the HO₂⁻ anion was optimized at the CCSD(T) level of theory with the d-aug-cc-pVQZ basis set using the Gaussian 09 suite of programs [62]. The added diffuse functions were included to describe the diffuse tails of the anion orbitals, as their long-range behaviour has a significant effect on the model PADs. The calculations predict that at its X^1A' equilibrium, HO_2^- has O-O and O-H bond lengths of 1.520 Å and 0.960 Å, respectively, and an H–O–O bond angle of 97.8°. The Dyson orbitals corresponding to the $X^1A' \to X^2A''$ and $X^1A' \to A^2A'$ photodetachment transitions were calculated for the above optimized geometry via the EOM-IP-CCSD method implemented in QChem 5.1 [63]. The canonical Hartree-Fock a" HOMO of HO₂⁻ and the Dyson orbital corresponding to the $X^1A' \rightarrow X^2A''$ photodetachment transition (nominally, removing an electron from the HOMO and therefore referred to, for brevity, as Dyson HOMO), are plotted side by side in Figure 4(a) and (b), respectively. The HF a'HOMO-1 and the Dyson orbital for the $X^1A' \rightarrow A^2A'$ photodetachment transition (Dyson HOMO-1), are similarly plotted in Figure 5(a) and (b), respectively. (Note the different orientations of the molecular frame in Figures 4 and 5). The orbitals bear clear resemblance to the p-d model function illustrated in Figure 1 and to each other, although under careful inspection the Dyson orbitals appear to be slightly more lopsided, compared to their HF counterparts.

The calculation outputs were used to generate custom $70 \times 70 \times 70$ cube files,

representing each MO as a three-dimensional array within a $(12 \text{ a.u.})^3$ volume, centred at the middle of the O-O bond. These cube files were imported into MATLAB and used for least-squares fits of the model function in the form of Eq. (1) to the *ab initio* orbitals. Using the axes definitions in Figure 1, the *p* and *d* parts of the model function were assumed to be real hydrogenic $2p_x$ and $3d_{zx}$ orbitals placed at the centre of the O-O bond. For the HOMO fit, the yz plane corresponded to the molecular plane; for HOMO-1, the zx plane played this role. The fits yielded the fractional *d* character, γ_d , and the charge parameters, ζ_{2p} and ζ_{3d} , for each of the four orbitals (Hartree-Fock HOMO and HOMO-1 and the Dyson orbitals for each). The fit parameters are summarized in the "MO cube fits" part of Table 1. The zx cross-sections of the resulting model functions are shown as contour plots in Figures 4 and 5, (c) and (d), for the HOMO and HOMO-1, HF and Dyson orbitals, respectively, where they can be compared to the isosurface plots of the corresponding *ab initio* orbitals shown above each contour plot.

The visual observation that each of the Dyson orbitals is slightly more polarized compared to the respective HF counterparts is reinforced by the smaller Dyson d character values. To stress this point, the γ_d values in Table 1 are converted to percent polarization, defined as magnitude of the p term coefficient in Eq. (1), $\sqrt{1-\gamma_d}$, expressed as percent. The small differences between the d characters of the HF and Dyson orbitals (0.979 vs. 0.945 for the HOMO and 0.871 vs. 0.788 for HOMO-1) translate into significant differences in polarization (14% vs. 23% for the HOMO and 36% vs. 46% for HOMO-1). These significant polarization values and the differences between them may surprize at first, because the orbitals themselves in Figures 4 and 5 do not look *that* lopsided or different from each other. The key to interpreting this observation is that the p polarization terms of the model functions correspond to significantly smaller charge-parameter values than the main d components (see Table 1), meaning

that the *p* terms are more diffuse and mostly affect the long-range amplitudes.

Next, Eq. (3) was used along with the A_1, A_2 , and B_2 formulas (6) to fit the p-d mixing model to the measured $\beta(\varepsilon)$ values. As discussed in Section 4.1, $\cos \delta_{2,0} = 0.95$ and $\cos \delta_{3,1} = 0.95$ were assumed. The fractional d characters were fixed at the values determined by fitting the model function to the corresponding MOs, while the ζ_{2p} and ζ_{3d} effective charges were used as free parameters. The resulting fits for the HOMO and HOMO–1 (HF and Dyson, each) are shown as dash-dotted black (for HF) and solid red (for Dyson) curves in Figure 3(a) and (b), respectively. The HF and Dyson fits are close to each other in each case, but not identical. Because of the slight difference in degrees of polarization within each pair of the HF and Dyson orbitals, the corresponding $\beta(\varepsilon)$ fits assume different γ_d values and hence yield distinct optimized charge parameters. The resulting ζ_{2p} and ζ_{3d} values are summarized in the "PAD data fits" part of Table 1.

Note that the charge parameters ζ_{2p} and ζ_{3d} for each orbital were determined twice, using two different approaches, with different results (compare the MO cube and PAD data parts of Table 1). This discrepancy is to be expected. The MO fit values reflect the structure of the orbitals within the limited range of the cube, capturing most of the electron density, but not providing an accurate description of the long-range behaviour of the orbitals. These fits do capture the asymmetric shapes of the orbitals and yield accurate estimates of the fractional d character, but the effective charges obtained from them do not describe the diffuse orbital "tails". Since it is the "tails" that the PADs are most sensitive to [41,64], the effective charges obtained from the MO fits are not particularly useful for modelling the PADs. The ζ_{2p} and ζ_{3d} values obtained from the fits of Eq. (3) to the $\beta(\varepsilon)$ experimental data, on the other hand, provide a more accurate description of the long-range behaviour of the MOs. Not surprisingly, the long-range charge values (from the PAD data fits) are consistently smaller than their short-

range counterparts (from the MO fits). This is because smaller effective charges correspond to more diffuse model functions.

4.3. Application of the model to O_2^- and NO^-

In order to compare the new HO₂⁻ results to O₂⁻ and NO⁻, it is necessary to perform similar analyses of these diatomic systems. For reference, the bond lengths in O₂⁻ and NO⁻, optimized the same way as HO₂⁻, are 1.349 Å and 1.266 Å, respectively, compared to a 1.520 Å O–O bond in HO₂⁻. The HOMOs of O₂⁻ and NO⁻ are shown in Figures 6 and 7, respectively. Similar to the presentation of the HO₂⁻ results, both HF and Dyson orbitals are shown in each case.

 O_2^- should be viewed as a reference system for the p-d model treatment of both HO_2^- and NO^- . In modelling the doubly degenerate π_g^* HOMO using Eq. (1), the p term strictly vanishes (by symmetry, $\gamma_d = 1$) and Eq. (3) reduces to the Hanstorp's adaptation [32] of the Cooper-Zare central-potential formula [28,29] with l = 2 [34-37]. Although it is not a true d orbital, the lowest-order contribution to its expansion beyond the d term is a g (l = 4) function, since the s, p, and f contributions all vanish by symmetry. Moving on from O_2^- to NO^- , molecular symmetry reduces from $D_{\infty h}$ to $C_{\infty v}$. The loss of the inversion centre results in the polarization of the NO^- HOMO, as seen in Figure 7, but does not affect its two-fold degeneracy. The degeneracy is lifted in HO_2^- , due to further symmetry reduction to C_s . Thus, the HOMO and HOMO-1 of HO_2^- both correlate to the doubly degenerate HOMOs of NO^- and O_2^- , making it appropriate to compare the detachment from both HO_2^- orbitals to the HOMO-1 transitions in NO^- and O_2^- .

We fit the p-d model function (1), with γ_d set to 1, to the cube arrays of the HF and Dyson variants of the O_2 ⁻ HOMO. Figures 6(c) and (d) show the cross-sections of

the optimized model functions, similar to the treatment of the HO2⁻ orbitals in Section 4.2. The corresponding ζ_{2p} and ζ_{3d} values are included in the "MO cube" part of Table 1. A snapshot of previously published $\beta(\varepsilon)$ data for O2⁻ from Ref. [57] is shown in Figure 8(a). To avoid complications due to strong vibronic coupling [36,57], the β values measured at various wavelengths for only the vertical transition, O2($X^3\Sigma_g^-$, v'=2) \leftarrow O2⁻($X^2\Pi_g$, v''=0), are included. Fits to these data using the Hanstorp-adapted [32] Cooper-Zare formula [28,29] with l=2 or, equivalently, Eq (3) with $\gamma_d=1$ yield $A_2=0.40(1)$ eV⁻¹ and $\cos\delta_{3,1}=0.95$ [57]. According to Eq. (6), the above A_2 value corresponds to $\zeta_{3d}=1.63(2)$, also included in Table 1. The least-squares fit of the model to the data in shown in Figure 8(a). In this case, there is no distinction between the fits using the parameters of the HF or Dyson HOMO, because both types of orbitals correspond to strictly the same γ_d value, $\gamma_d=1$, and hence the corresponding fits of Eq. (3) to the data converge on the same result.

Turning to NO⁻, the *p-d* model functions obtained by fitting Eq. (1) to the HF and Dyson variants of the HOMO [Figures 7(a) and (b)] are represented by their cross-sections in Figures 7(c) and (d), respectively. The corresponding fit parameters are included in Table 1. A snapshot of NO⁻ $\beta(\varepsilon)$ data is given in Figure 8(b) [41,65-67]. There is strong vibronic coupling in this case as well, so again only the vertical transition, NO($X^2\Pi$, v'=2) \leftarrow NO⁻($X^3\Sigma^-$, v''=0), is represented in the figure. The least-squares fits of Eq. (3), using the same process as for HO₂⁻, i.e. with $\cos\delta_{2,0}=0.95$, $\cos\delta_{3,1}=0.95$, and γ_d determined from the MO fits above ($\gamma_d=0.985$ for the HF HOMO and $\gamma_d=0.965$ for the Dyson orbital), yield the respective dash-dotted black and solid red curves in Figure 8(b). The charge parameters are included in Table 1.

5. Discussion

5.1. Hartree-Fock vs. Dyson orbitals

We have compared the canonical Hartree-Fock and correlated Dyson orbitals of HO₂⁻, NO⁻, and O₂⁻ [Figures 4-7, parts (a) and (b), respectively]. In general, Dyson orbitals are the rigorously appropriate functions for describing photodetachment. Although HF orbitals often do provide a good approximation, they are prone to yielding qualitatively incorrect pictures in some cases, for example, when the energetic ordering of the orbitals/states is affected by electron correlation [46]. Thanks to the availability of modern computational packages [63], calculating Dyson orbitals has become fairly straightforward. It needs to be said, however, that canonical HF orbitals continue to hold appeal, not only due to reduced computational complexity and broader familiarity in the chemistry community, but also because they provide a (however incomplete) bonding picture of the anions themselves. In contrast, by their very definition, Dyson orbitals describe the overlap between the anion and neutral wavefunctions and, therefore, reflect the properties of the transition, not the anion.

In all cases discussed in this work, the HF and Dyson orbitals closely resemble each other and provide consistent and complementary insight into the observed PADs. This observation complements a similar conclusion reached in the application of the *s-p* variant of the mixed-character model [37,39]. It warrants mentioning, however, that for all three distorted *d*-like orbitals discussed here (the HOMO and HOMO–1 of HO2⁻ and the HOMO of NO⁻), the Dyson orbitals are noticeably more polarized than their HF counterparts, as borne out by the γ_d values, indicated in parts (c) and (d) of Figures 4, 5, and 7, and in Table 1. This observation does not have a significant effect on the ultimate modelling of the PADs using the *p-d* model—the "HF" and "Dyson" curves in Figures

3 and 8 fall very close to each other—but that is only because the differences between the respective d characters plugged into Eq. (3) are offset by the corresponding adjustments of the ζ_{2p} and ζ_{3d} charge parameters.

In the case of HO₂⁻, we have also compared the output of the p-d model to the predictions of the ezDyson program developed by Gozem and Krylov [68]. The outputs of the QChem EOM-IP-CCSD/d-aug-pVQZ calculations, including the Dyson orbitals shown in Figures 4(b) and 5(b), were imported into ezDyson and the energy-dependent photoelectron anisotropy values were calculated for each of the transitions by expanding the continuum state of the electron in partial waves up to l_f = 5 (changing this limit to l_f = 7 did not have an appreciable effect on the results). The resulting $\beta(\varepsilon)$ curves are included in Figures 3(a) and (b), shown as dashed blue lines labelled "ezDyson".

Overall, the ezDyson calculations reproduce the observed experimental trends quite well. The apparently better agreement of the "HF" and "Dyson" *p-d* model curves with the experimental data does not indicate a better performance of the model compared to ezDyson. In fact, such quality comparison should not be made at all. The *p-d* model curves agree with the data so well, because Eq. (3) was fit to the experimental results. The ezDyson curves, on the other hand, are purely *ab initio* predictions, obtained with no reliance on the experimental data shown. This highlights the fundamental difference between the two approaches. ezDyson predicts PADs from first principles, based on the calculated electronic structure of the parent anion. The mixed-character model, on the other hand, works in the opposite direction: its goal is not to predict the experimental results, but to provide a means for their interpretation. By reducing the photodetachment orbitals to superpositions of just two basis functions and expressing the PADs in terms of model parameters that are common in elementary electronic structure (such as effective charges), the model helps interpret what the observed PADs

mean, i.e. what they imply about the dominant character of the parent anion orbitals and hence the anions themselves.

5.2. Out-of-plane HOMO vs. in-plane HOMO-1 of HO₂⁻

For reasons discussed in Section 4.2, in the following discussion, we focus on the long-range ζ_{2p} and ζ_{3d} values obtained by fitting the p-d model formula (3) to the experimental data, along with the γ_d values determined from the MO cube fits. These quantities are bolded in Table 1. The HOMO and HOMO-1 of HO2⁻ (Figures 4 and 5) both look like lopsided d-like orbitals. While neither is truly a d or a p-d orbital, both possess clear p-d character and are best described as distorted, but predominantly d-like functions. The p term in Eq. (1) captures the first-order effect of the distortion. Since the ζ_{2p} values for both orbitals are smaller than the corresponding ζ_{3d} charges (Table 1), the polarization terms are significantly more diffuse than the dominant d components.

The qualitative similarity of the two orbitals is especially revealing in the context of their different symmetry species: A" for the HOMO vs. A' for the HOMO-1. If one were to reduce the MOs just to their symmetry representations, qualitatively different PADs would be predicted for the two of them. For example, the qualitative symmetry-only-based s&p model [48,69] (not to be confused with s-p mixing [38]), predicts negative β values for detachment from the HOMO, in agreement with the results in Figure 3(a), and β of for the HOMO-1, contrary to Figure 3(b). Thus, the different symmetry characters of the two orbitals are not reflected in the PADs and the present analysis explains why: despite their different representations, the HOMO and HOMO-1 of HO₂- are qualitatively similar. The HOMO/HOMO-1 degeneracy is lifted due to the off-O-O-axis presence of the H atom, which also accounts for the different symmetry species and slightly different shapes of the two MOs. Yet, there is little or no

MO density of the hydrogen in both orbitals: in the LCAO-MO picture, they consist predominantly of oxygens' 2p orbitals. Thus, the symmetry species should not be part of a qualitative analysis of photodetachment from these otherwise similar orbitals, because the difference in symmetry is due to an atom which hardly contributes to (is decoupled from) the orbitals themselves.

Despite the qualitative similarity, the quantitative differences between the HOMO and HOMO-1 are nonetheless observable. Based on the γ_d values (Table 1), the distortion/polarization p term in the HF/Dyson HOMO is about 2%/5% by population or 14%/23% by amplitude, while that in the HF/Dyson HOMO-1 is 13%/21% by population or 36%/46% by amplitude. From the bonding perspective, the addition of the O-H bond to O_2 - lifts the degeneracy of superoxide's d-like HOMO, splitting it into the distinct HOMO and HOMO-1 of HO_2 -. With the hydrogen atom located in the plane of the HOMO-1, its polarizing effect on the otherwise d-like MO is more significant, compared to the HOMO, as clearly borne out by the above p terms amplitudes. The a' HOMO-1 also possesses partial σ bonding character with respect to the O-H bond, which is absent (by symmetry) in the a'' HOMO. This partial bonding character of the HOMO-1 versus the throughout π antibonding character of the HOMO, explains the energetic ordering of the two MOs.

5.3. The O_2^- vs. NO^- vs. HO_2^- series

Since the introduction of Hanstorp's A_l parameters [32], it was understood that their magnitude is related to the "size" of the anion. With the "size" defined by the spatial extent of the outermost orbital, this relationship is clearly borne out in Eq. (6). For *d*-like orbitals, the inverse-square dependence of A_2 on ζ_{3d} dictates that the larger—the more diffuse—the anion, the smaller the ζ_{3d} values, and the larger the A_2 magnitude.

The anion's "size" is also related to its binding energy. Tighter-bound anions have more compact orbitals, while weakly bound systems are more diffuse. Dipole- or correlation-bound anions are the ultimate examples of the latter, while a completely delocalized free electron in the presence of a neutral molecule serves is an asymptotic limit corresponding to an infinitely large "anion" with zero binding energy.

Generalizing these observations, the "size" of the anion is, in general, positively correlated with the appropriate A_l coefficients and negatively correlated with the effective charges ζ_{nl} and the eBE. These correlations are not linear and also dependent on other factors (such as, for example, the molecular geometry). However, they do give correct intuitive insight both into the chemistry of electron binding and the physics of the photodetachment process. This conceptual level of insight is the motivation behind the present work and the original development of the mixing model [41].

In the O_2^- , NO^- , and HO_2^- series, the electron binding energies increase from NO^- , for which the adiabatic EA of NO is 0.04 eV [65], to O_2^- (EA of O_2 is 0.45 eV [70]), to HO_2^- (EA of HO_2 is 1.089 eV, from Refs. [19,22] and this work). The HOMOs of all three anions are predominantly d-like functions with various degrees of symmetry-dependent distortions. Therefore, the ζ_{3d} effective charges (Table 1) can be used as a measure of these anions' "size". Comparing O_2^- to HO_2^- , we notice that the electron binding energy increases in direct correlation with ζ_{3d} , as expected based on the above arguments. We do also notice that ζ_{3d} values for the (HF or Dyson) HOMO-1 in HO_2^- are similar or smaller than for the HOMO, which is counterintuitive, because the binding energy of HOMO-1 is greater than that of the HOMO. However, the a' HOMO-1 lies in the HOO molecular plane and includes a partial (small) bonding character with respect to the O-H bond. The a'' HOMO, on the other hand, is an out-of-plane orbital localized strictly on the diatomic O-O moiety. These differences, accounting for the in-

plane HOMO-1 being geometrically larger, compared to the HOMO, are responsible for the ζ_{3d} values breaking the binding-energy trend.

Comparing NO⁻ to O₂⁻ reveals another insightful discrepancy. Despite the electron binding energy to NO being smaller than to O₂, the corresponding ζ_{3d} values are similar. In fact, both HF and Dyson NO⁻ values are slightly larger, seemingly suggesting that the NO⁻ HOMO is less diffuse than that of O₂⁻. Recall, however, that in contrast to O₂⁻ the NO⁻ HOMO is a lopsided orbital, as accounted for by a very diffuse $(\zeta_{2p} = 0.70/0.77 \text{ vs. } \zeta_{3d} = 1.78/1.80) p$ contribution. The difference between ζ_{2p} and ζ_{3d} implies that the polarizing effect is more significant in the diffuse regions of the orbital. Although the weight of the p component is small (1.5%/3.5% by population, 12%/19% by amplitude), the PADs have been shown to be most sensitive to the diffuse parts of the parent wavefunction [41,64], boosting the contribution of the p term to the data. Thus, the appropriate comparison is not $\zeta_{3d} = 1.63$ for O₂⁻ vs. $\zeta_{3d} = 1.78/1.80$ for NO⁻, but $\zeta_{3d} = 1.63$ for O₂⁻ vs. some moment of $\zeta_{2p} = 0.70/0.77$ and $\zeta_{3d} = 1.78/1.80$ for NO⁻, where the weight of ζ_{2p} is more significant than suggested by γ_d .

6. Summary

We presented a comprehensive imaging study of the photoelectron angular distributions in HO₂⁻ photodetachment. The results were analysed using the *p-d* variant of the general mixed-character model [41] and compared to NO⁻ and O₂⁻ photodetachment. The comparison sheds light on the effects of molecular symmetry and chemical bonding structures on the photodetachment process and the PADs.

In the context of the p-d model, the initial bound state of the electron (i.e., the parent MO) or the corresponding Dyson orbital is described as a superposition of atomic p and d basis functions placed at a chosen centre in the molecular frame. As the PADs

are sensitive to the long-range scaling of the diffuse tails of the MOs, the asymptotic behaviour of the model function is of key importance to the analysis. This behaviour was parameterized in terms of the effective charges ζ_{2p} and ζ_{3d} , which do not correspond to any physical charges within the anion, but describe the long-range scaling of the model function and the MO. Using the formalism developed elsewhere [41], the observed PADs and their variation with eKE are defined by three parameters: the above effective charges and the fractional d character parameterizing the symmetry-adapted structure of the parent orbital.

The model results and the predicted trend within the O₂-, NO-, and HO₂- anion series are consistent with physical intuition and the known trends in other physical observables, such as the electron binding or anion detachment energies.

ACKNOWLEDGEMENTS

This work was made possible by funding from the U.S. National Science Foundation, Grant CHE-1664732. We thank Mikhail Ryazanov for his help with the circularization tool of the PyAbel program [53]. Part of this work was conducted using the resources [68] of the iOpenShell Center for Computational Studies of Electronic Structure and Spectroscopy of Open-Shell and Electronically Excited Species (http://iopenshell.usc.edu).

Table 1. Model parameters for the HOMO and HOMO-1 of HO₂⁻ and the respective doubly degenerate HOMOs of O₂⁻ and NO⁻.

Anion/Orbital	MO cube fits			Percent	PAD data fits	
	ζ_{2p}^{a}	ζ_{3d}^{a}	γ_d a	polari- zation ^b	$\zeta_{2p}^{\ \ c}$	ζ3 <i>d</i> ^c
HO ₂ -						
HOMO Hartree-Fock Dyson HOMO–1 Hartree-Fock	1.59 1.88 2.09	4.71 4.64 4.54	0.979 0.945 0.871	14% 23%	1.01(4) 1.18(4) 1.0(2)	2.53(8) 2.63(9) 2.2(4)
Dyson	2.16	4.53	0.788	46%	1.1(2)	2.4(6)
O ₂ ⁻ HOMO Hartree-Fock Dyson	_ _	5.20 4.99	1 1	0% 0%	- -	1.63(2) 1.63(2)
NO ⁻ HOMO Hartree-Fock Dyson	1.67 1.25	5.10 4.85	0.985 0.965	12% 19%	0.70(4) 0.77(4)	1.78(9) 1.80(7)

^a Parameter values determined by fitting the *p-d* model function (1) to the *ab initio* (HF or Dyson) orbitals.

Percent polarization describes the amplitude of the p polarization term in the p-d model function (1), defined as $\sqrt{1-\gamma_d} \times 100\%$.

^c These ζ_{2p} and ζ_{3d} values were determined by fitting the model equation (3) to the experimental data, with γ_d constrained to the values from the corresponding MO fits.

REFERENCES

- [1] P. S. Monks, Chem. Soc. Rev. 34, 376 (2004).
- [2] M. Duncianu, A. Lahib, A. Tomas, P. S. Stevens, and S. Dusanter, *Atmos. Environ.* **222** (2020).
- [3] K. A. Read, A. C. Lewis, S. Bauguitte, A. M. Rankin, R. A. Salmon, E. W. Wolff, A. Saiz-Lopez, W. J. Bloss, D. E. Heard, J. D. Lee, and J. M. C. Plane, *Atmos. Chem. Phys.* **8**, 2985 (2008).
- [4] J. Mao, D. J. Jacob, M. J. Evans, J. R. Olson, X. Ren, W. H. Brune, J. M. St Clair, J. D. Crounse, K. M. Spencer, M. R. Beaver, P. O. Wennberg, M. J. Cubison, J. L. Jimenez, A. Fried, P. Weibring, J. G. Walega, S. R. Hall, A. J. Weinheimer, R. C. Cohen, G. Chen, J. H. Crawford, C. McNaughton, A. D. Clarke, L. Jaegle, J. A. Fisher, R. M. Yantosca, P. Le Sager, and C. Carouge, *Atmos. Chem. Phys.* 10, 5823 (2010).
- [5] R. Volkamer, P. Sheehy, L. T. Molina, and M. J. Molina, *Atmos. Chem. Phys.* **10**, 6969 (2010).
- [6] S. Dusanter, D. Vimal, P. S. Stevens, R. Volkamer, L. T. Molina, A. Baker, S. Meinardi, D. Blake, P. Sheehy, A. Merten, R. Zhang, J. Zheng, E. C. Fortner, W. Junkermann, M. Dubey, T. Rahn, B. Eichinger, P. Lewandowski, J. Prueger, and H. Holder, *Atmos. Chem. Phys.* **9**, 6655 (2009).
- [7] G. M. Wolfe, J. A. Thornton, M. McKay, and A. H. Goldstein, *Atmos. Chem. Phys.* **11**, 7875 (2011).
- [8] S. M. Griffith, R. F. Hansen, S. Dusanter, P. S. Stevens, M. Alaghmand, S. B. Bertman, M. A. Carroll, M. Erickson, M. Galloway, N. Grossberg, J. Hottle, J. Hou, B. T. Jobson, A. Kammrath, F. N. Keutsch, B. L. Lefer, L. H. Mielke, A. O'Brien, P. B. Shepson, M. Thurlow, W. Wallace, N. Zhang, and X. L. Zhou, *Atmos. Chem. Phys.* 13, 5403 (2013).
- [9] A. T. Archibald, J. G. Levine, N. L. Abraham, M. C. Cooke, P. M. Edwards, D. E. Heard, M. E. Jenkin, A. Karunaharan, R. C. Pike, P. S. Monks, D. E. Shallcross, P. J. Telford, L. K. Whalley, and J. A. Pyle, *Geophys. Res. Lett.* **38** (2011).
- [10] D. J. Creasey, G. E. Evans, D. E. Heard, and J. D. Lee, *J. Geophys. Res.-Atmos.* **108**, 4475 (2003).
- [11] H. Berresheim, T. Elste, H. G. Tremmel, A. G. Allen, H. C. Hansson, K. Rosman, M. Dal Maso, J. M. Makela, M. Kulmala, and C. D. O'Dowd, *J. Geophys. Res.-Atmos.* **107** (2002).
- [12] S. Iyer, H. Reiman, K. H. Moller, M. P. Rissanen, H. G. Kjaergaard, and T. Kurten, *J. Phys. Chem. A* **122**, 9542 (2018).
- [13] J. M. St Clair, J. C. Rivera-Rios, J. D. Crounse, H. C. Knap, K. H. Bates, A. P. Teng, S. Jorgensen, H. G. Kjaergaard, F. N. Keutsch, and P. O. Wennberg, *J. Phys. Chem. A* **120**, 1441 (2016).
- [14] J. M. Anglada, M. Torrent-Sucarrat, M. F. Ruiz-Lopez, and M. Martins-Costa, *Chem. Eur. J.* **18**, 135435 (2012).
- [15] G. Merenyi, J. Lind, S. Naumov, and C. von Sonntag, *Chem. Eur. J.* **16**, 1372 (2010).
- [16] S. M. Griffith, R. F. Hansen, S. Dusanter, V. Michoud, J. B. Gilman, W. C. Kuster, P. R. Veres, M. Graus, J. A. de Gouw, J. Roberts, C. Young, R. Washenfelder, S. S. Brown, R. Thalman, E. Waxman, R. Volkamer, C. Tsai, J. Stutz, J. H. Flynn, N. Grossberg, B. Lefer, S. L. Alvarez, B. Rappenglueck, L. H. Mielke, H. D. Osthoff, and P. S. Stevens, *J. Geophys. Res.-Atmos.* 121, 4211 (2016).

- [17] S. R. Albrecht, A. Novelli, A. Hofzumahaus, S. Kang, Y. Baker, T. Mentel, A. Wahner, and H. Fuchs, *Atmos. Measur. Tech.* **12**, 891 (2019).
- [18] J. Sanchez, D. J. Tanner, D. X. Chen, L. G. Huey, and N. L. Ng, *Atmos. Measur. Tech.* **9**, 3851 (2016).
- [19] E. P. Clifford, P. G. Wenthold, R. Gareyev, W. C. Lineberger, C. H. DePuy, V. M. Bierbaum, and G. B. Ellison, *J. Chem. Phys.* **109**, 10293 (1998).
- [20] J. M. Oakes, L. B. Harding, and B. G. Ellison, J. Chem. Phys. 83, 5400 (1985).
- [21] M. E. Jacox, J. Phys. Chem. Ref. Data, 1 (1994).
- [22] R. P. Tuckett, P. A. Freedman, and W. J. Jones, Mol. Phys. 37, 379 (1979).
- [23] K. H. Becker, E. H. Fink, P. Langen, and U. Schurath, *J. Chem. Phys.* **60**, 4623 (1974).
- [24] A. T. J. B. Eppink and D. H. Parker, Rev. Sci. Instrum. 68, 3477 (1997).
- [25] D. H. Parker and A. T. J. B. Eppink, J. Chem. Phys. 107, 2357 (1997).
- [26] D. W. Chandler and P. L. Houston, J. Chem. Phys. 87, 1445 (1987).
- [27] A. J. R. Heck and D. W. Chandler, Annu. Rev. Phys. Chem. 46, 335 (1995).
- [28] J. Cooper and R. N. Zare, J. Chem. Phys. 48, 942 (1968).
- [29] J. Cooper and R. N. Zare, J. Chem. Phys. 49, 4252 (1968).
- [30] J. Cooper and R. N. Zare, in *Atomic collision processes*, edited by S. Geltman, K. T. Mahanthappa, and W. E. Brittin (Gordon and Breach, Science Publishers, New York, London, Paris, 1968), Vol. XI-C pp. 317-337.
- [31] H. A. Bethe and E. E. Salpeter, *Quantum Mechanics of One- and Two-Electron Atoms* (Springer-Verlag; Academic Press Inc., Berlin; New York, 1957), p. 368.
- [32] D. Hanstorp, C. Bengtsson, and D. J. Larson, *Phys. Rev. A* 40, 670 (1989).
- [33] E. P. Wigner, *Phys. Rev.* **73**, 1002 (1948).
- [34] D. S. Burch, S. J. Smith, and L. M. Branscomb, *Phys. Rev.* 112, 171 (1958).
- [35] K. J. Reed, A. H. Zimmerman, H. C. Andersen, and J. I. Brauman, *J. Chem. Phys.* **64**, 1368 (1976).
- [36] R. Mabbs, F. Mbaiwa, J. Wei, M. Van Duzor, S. T. Gibson, S. J. Cavanagh, and B. R. Lewis, *Phys. Rev. A* **82**, 011401 (2010).
- [37] A. Sanov, Annu. Rev. Phys. Chem. 65, 341 (2014).
- [38] E. R. Grumbling and A. Sanov, J. Chem. Phys. 135, 164302 (2011).
- [39] L. M. Culberson, C. C. Blackstone, and A. Sanov, *J. Phys. Chem. A* **117**, 11760 (2013).
- [40] L. M. Culberson, C. C. Blackstone, A. A. Wallace, and A. Sanov, *J. Phys. Chem. A* **119**, 9770 (2015).
- [41] D. Khuseynov, C. C. Blackstone, L. M. Culberson, and A. Sanov, *J. Chem. Phys.* **141**, 124312 (2014).
- [42] F. A. Akin, L. K. Schirra, and A. Sanov, J. Phys. Chem. A 110, 8031 (2006).
- [43] J. V. Ortiz, Int. J. Quantum Chem 100, 1131 (2004).
- [44] C. M. Oana and A. I. Krylov, J. Chem. Phys. 127, 234106 (2007).
- [45] C. M. Oana and A. I. Krylov, J. Chem. Phys. 131, 124114 (2009).
- [46] A. I. Krylov, J. Chem. Phys. 153, 080901 (2020).
- [47] K. M. Ervin and W. C. Lineberger, in *Advances in Gas Phase Ion Chemistry*, edited by N. G. Adams and L. M. Babcock (JAI Press, Greenwich, 1992), Vol. 1 pp. 121-166.
- [48] E. Surber and A. Sanov, J. Chem. Phys. 116, 5921 (2002).
- [49] R. Mabbs, E. Surber, and A. Sanov, *Analyst* **128**, 765 (2003).
- [50] H.-X. Lin, H.-L. Liang, G.-H. Chen, F.-L. Gu, W.-G. Liu, and S.-F. Ni, *J. Phys. Chem. A* **116**, 11656 (2012).

- [51] A. Midey, I. Dotan, J. V. Seeley, and A. A. Viggiano, *Int. J. Mass Spectrom.* **280**, 6 (2009).
- [52] W. C. Wiley and I. H. McLaren, Rev. Sci. Instrum. 26, 1150 (1955).
- [53] S. Gibson, D. D. Hickstein, R. Yurchak, M. Ryazanov, D. Dhrubajyoti, and S. Gilbert, *PyAbel:* v0.8.3 (GitHub, 2019).
- [54] J. R. Gascooke, S. T. Gibson, and W. D. Lawrance, *J. Chem. Phys.* **147**, 013924 (2017).
- [55] V. Dribinski, A. Ossadtchi, V. A. Mandelshtam, and H. Reisler, *Rev. Sci. Instrum.* 73, 2634 (2002).
- [56] R. Mabbs, E. Surber, and A. Sanov, *J. Chem. Phys.* **122**, 054308 (2005).
- [57] M. Van Duzor, F. Mbaiwa, J. Wei, T. Singh, R. Mabbs, A. Sanov, S. J. Cavanagh, S. T. Gibson, B. R. Lewis, and J. R. Gascooke, *J. Chem. Phys.* **133**, 174311 (2010).
- [58] R. S. Mulliken, J. Chem. Phys. 23, 1833 (1955).
- [59] F. L. Hirshfeld, Theoretica Chimica Acta 44, 129 (1977).
- [60] J. C. Slater, Phys. Rev. 36, 57 (1930).
- [61] E. Clementi and D. L. Raimondi, J. Chem. Phys. 38, 2686 (1963).
- [62] M. J. Frisch, G. W. Trucks, H. B. Schlegel, G. E. Scuseria, M. A. Robb, J. R. Cheeseman, G. Scalmani, V. Barone, B. Mennucci, G. A. Petersson, H. Nakatsuji, M. Caricato, X. Li, H. P. Hratchian, A. F. Izmaylov, J. Bloino, G. Zheng, J. L. Sonnenberg, M. Hada, M. Ehara, K. Toyota, R. Fukuda, J. Hasegawa, M. Ishida, T. Nakajima, Y. Honda, O. Kitao, H. Nakai, T. Vreven, J. Montgomery, J. A., J. E. Peralta, F. Ogliaro, M. Bearpark, J. J. Heyd, E. Brothers, K. N. Kudin, V. N. Staroverov, R. Kobayashi, J. Normand, K. Raghavachari, A. Rendell, J. C. Burant, S. S. Iyengar, J. Tomasi, M. Cossi, N. Rega, N. J. Millam, M. Klene, J. E. Knox, J. B. Cross, V. Bakken, C. Adamo, J. Jaramillo, R. Gomperts, R. E. Stratmann, O. Yazyev, A. J. Austin, R. Cammi, C. Pomelli, J. W. Ochterski, R. L. Martin, K. Morokuma, V. G. Zakrzewski, G. A. Voth, P. Salvador, J. J. Dannenberg, S. Dapprich, A. D. Daniels, Ö. Farkas, J. B. Foresman, J. V. Ortiz, J. Cioslowski, and D. J. Fox, Gaussian 09 (Gaussian, Inc., Wallingford, CT, 2009).
- [63] Y. H. Shao, Z. T. Gan, E. Epifanovsky, A. T. B. Gilbert, M. Wormit, J. Kussmann, A. W. Lange, A. Behn, J. Deng, X. T. Feng, D. Ghosh, M. Goldey, P. R. Horn, L. D. Jacobson, I. Kaliman, R. Z. Khaliullin, T. Kus, A. Landau, J. Liu, E. I. Proynov, Y. M. Rhee, R. M. Richard, M. A. Rohrdanz, R. P. Steele, E. J. Sundstrom, H. L. Woodcock, P. M. Zimmerman, D. Zuev, B. Albrecht, E. Alguire, B. Austin, G. J. O. Beran, Y. A. Bernard, E. Berquist, K. Brandhorst, K. B. Bravaya, S. T. Brown, D. Casanova, C. M. Chang, Y. O. Chen, S. H. Chien, K. D. Closser, D. L. Crittenden, M. Diedenhofen, R. A. DiStasio, H. Do, A. D. Dutoi, R. G. Edgar, S. Fatehi, L. Fusti-Molnar, A. Ghysels, A. Golubeva-Zadorozhnaya, J. Gomes, M. W. D. Hanson-Heine, P. H. P. Harbach, A. W. Hauser, E. G. Hohenstein, Z. C. Holden, T. C. Jagau, H. J. Ji, B. Kaduk, K. Khistyaev, J. Kim, J. Kim, R. A. King, P. Klunzinger, D. Kosenkov, T. Kowalczyk, C. M. Krauter, K. U. Lao, A. D. Laurent, K. V. Lawler, S. V. Levchenko, C. Y. Lin, F. Liu, E. Livshits, R. C. Lochan, A. Luenser, P. Manohar, S. F. Manzer, S. P. Mao, N. Mardirossian, A. V. Marenich, S. A. Maurer, N. J. Mayhall, E. Neuscamman, C. M. Oana, R. Olivares-Amaya, D. P. O'Neill, J. A. Parkhill, T. M. Perrine, R. Peverati, A. Prociuk, D. R. Rehn, E. Rosta, N. J. Russ, S. M. Sharada, S. Sharma, D. W. Small, A. Sodt, T. Stein, D. Stuck, Y. C. Su, A. J. W. Thom, T. Tsuchimochi, V. Vanovschi, L. Vogt, O. Vydrov, T. Wang, M. A. Watson, J. Wenzel, A. White, C. F. Williams, J. Yang, S. Yeganeh, S. R. Yost, Z. Q. You, I. Y. Zhang, X. Zhang,

- Y. Zhao, B. R. Brooks, G. K. L. Chan, D. M. Chipman, C. J. Cramer, W. A. Goddard, M. S. Gordon, W. J. Hehre, A. Klamt, H. F. Schaefer, M. W. Schmidt, C. D. Sherrill, D. G. Truhlar, A. Warshel, X. Xu, A. Aspuru-Guzik, R. Baer, A. T. Bell, N. A. Besley, J. D. Chai, A. Dreuw, B. D. Dunietz, T. R. Furlani, S. R. Gwaltney, C. P. Hsu, Y. S. Jung, J. Kong, D. S. Lambrecht, W. Z. Liang, C. Ochsenfeld, V. A. Rassolov, L. V. Slipchenko, J. E. Subotnik, T. Van Voorhis, J. M. Herbert, A. I. Krylov, P. M. W. Gill and M. Head-Gordon, *Mol. Phys.* 113, 184 (2015).
- [64] A. Sanov, E. R. Grumbling, D. J. Goebbert, and L. M. Culberson, *J. Chem. Phys.* **138**, 054311 (2013).
- [65] L. Velarde, T. Habteyes, E. R. Grumbling, K. Pichugin, and A. Sanov, *J. Chem. Phys.* **127**, 084302 (2007).
- [66] E. R. Grumbling, K. Pichugin, L. Velarde, and A. Sanov, *J. Phys. Chem. A* **114**, 1367 (2010).
- [67] E. R. Grumbling, R. Mabbs, and A. Sanov, J. Chem. Educ. 88, 1515 (2011).
- [68] S. Gozem and A. I. Krylov, *ezDyson*, http://iopenshell.usc.edu/downloads/ezdyson.
- [69] E. Surber, R. Mabbs, and A. Sanov, J. Phys. Chem. A 107, 8215 (2003).
- [70] K. M. Ervin, W. Anusiewicz, P. Skurski, J. Simons, and W. C. Lineberger, *J. Phys. Chem. A* **107**, 8521 (2003).

Figure 1

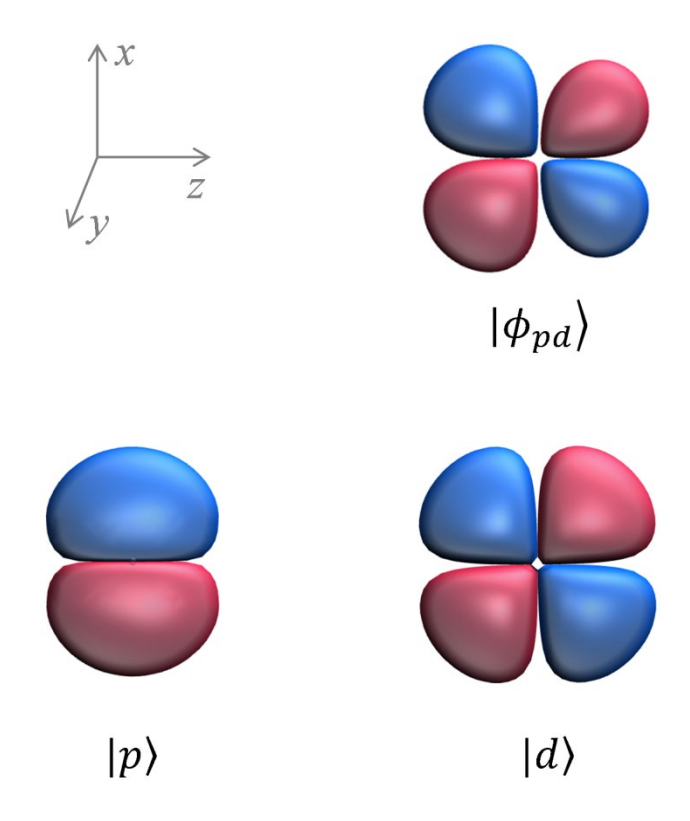


Figure 1. Illustration of the p-d variant of the mixing model. Shown in the top left are the molecular-frame Cartesian coordinate axes. $|\phi_{pd}\rangle$ is a model mixed p-d orbital defined in Eq. (1). $|p\rangle$ and $|d\rangle$ are the corresponding components of the mixed p-d state, in this example represented specifically by the $2p_x$ and $3d_{zx}$ atomic-orbital functions located at the same centre.

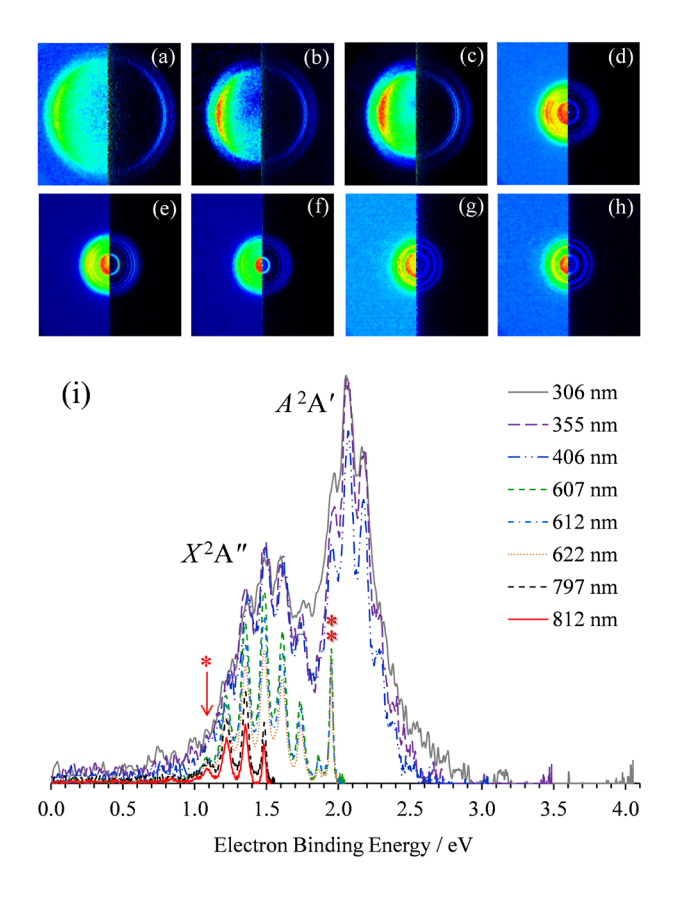


Figure 2. Top: Raw (left) and inverse Abel transformed (right) photoelectron images of HO_2^- collected at (a) 306 nm, (b) 355 nm, (c) 406 nm, (d) 622 nm, (e) 612 nm, (f) 607 nm, (g) 797 nm, and (h) 812 nm. Bottom: (i) Photoelectron spectra corresponding to the images (a)-(h). The single asterisk marks the origin peak of the $X^2A'' \leftarrow X^1A'$ transition, while the double asterisk marks the origin of the first excited state, A^2A' .

Figure 3

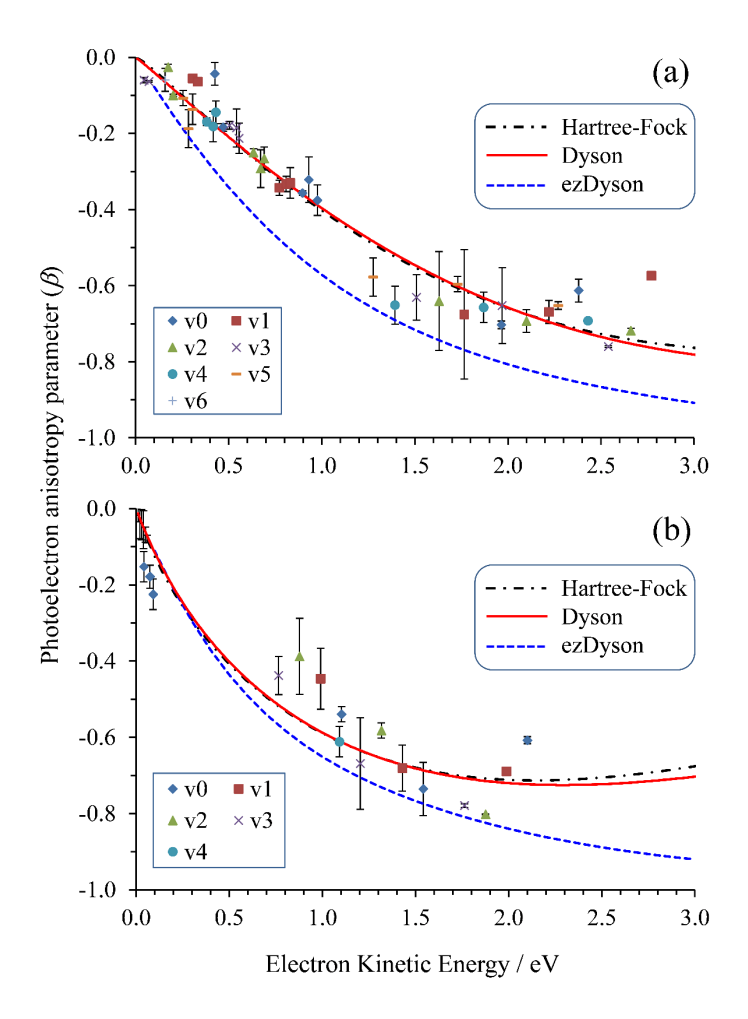


Figure 3. Anisotropy parameter β as a function of electron kinetic energy for photode-tachment from the (a) HOMO and (b) HOMO-1 of HO₂⁻, corresponding to the X^2A'' and A^2A' electronic states of the resulting HO₂ radical. The v0, v1, etc. labels correspond to the v'=0, 1, etc. vibrational states of the neutral HO₂. Solid curves represent the fits to the experimental data using p-d model equation (3) with the γ_d values constrained as follows. In (a), $\gamma_d=0.979$ for the Hartree-Fock MO (dash-dotted black curve) and $\gamma_d=0.945$ for the Dyson orbital (solid red curve). In (b), $\gamma_d=0.871$ for the Hartree-Fock MO (dash-dotted black curve) and $\gamma_d=0.788$ for the Dyson orbital (solid red curve). The resulting ζ_{2p} and ζ_{3d} values are given in the PAD data fits part of Table 1. The dashed blue curves in (a) and (b) are the corresponding ab initio predictions obtained using the ezDyson program.

Figure 4

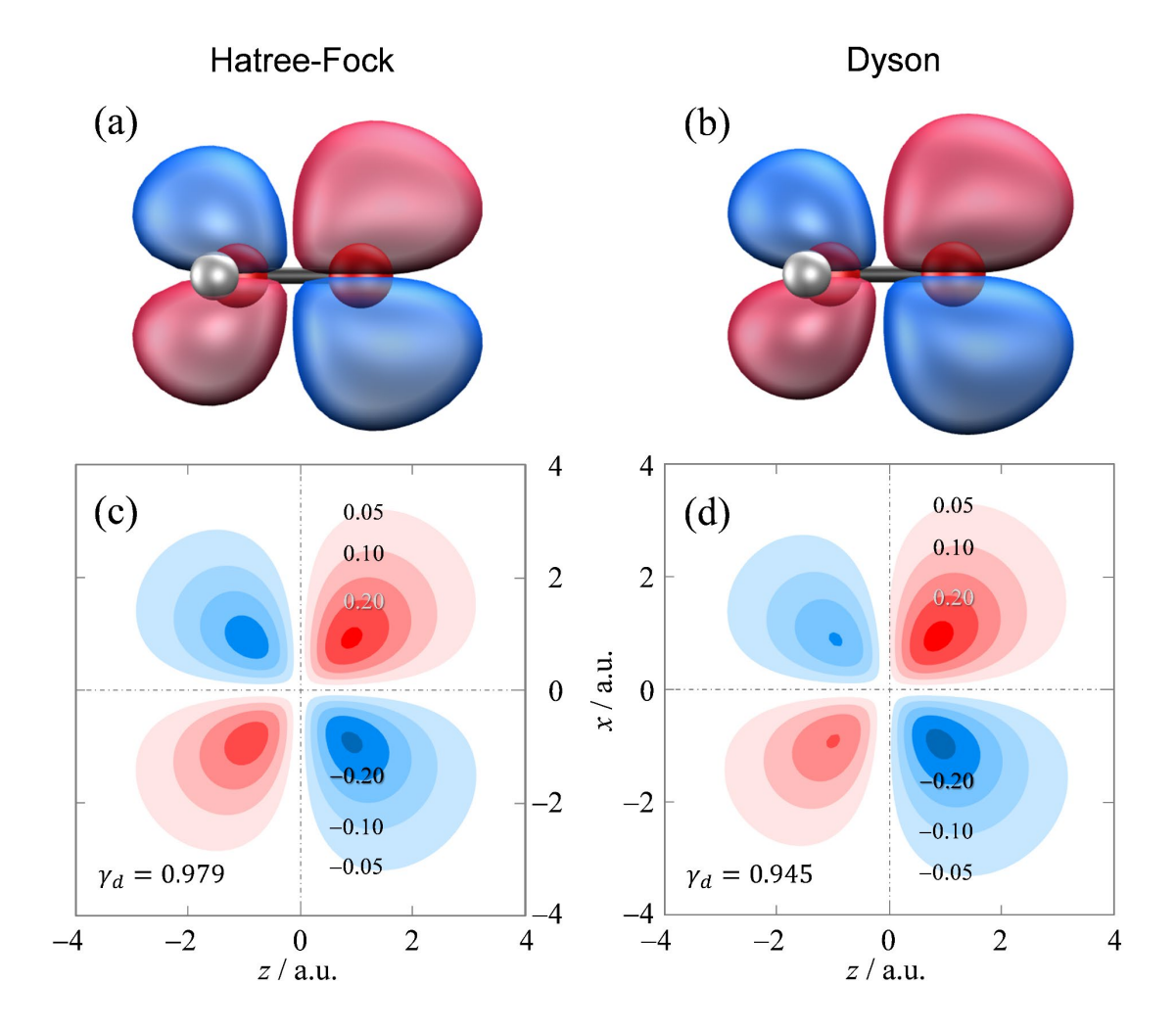


Figure 4. (a) Canonical HF and (b) Dyson orbitals, corresponding to photodetachment from the a'' HOMO of HO_2^- . (c)-(d) Cross-sections of the model functions defined by equation (1), representing the above orbitals.

Figure 5

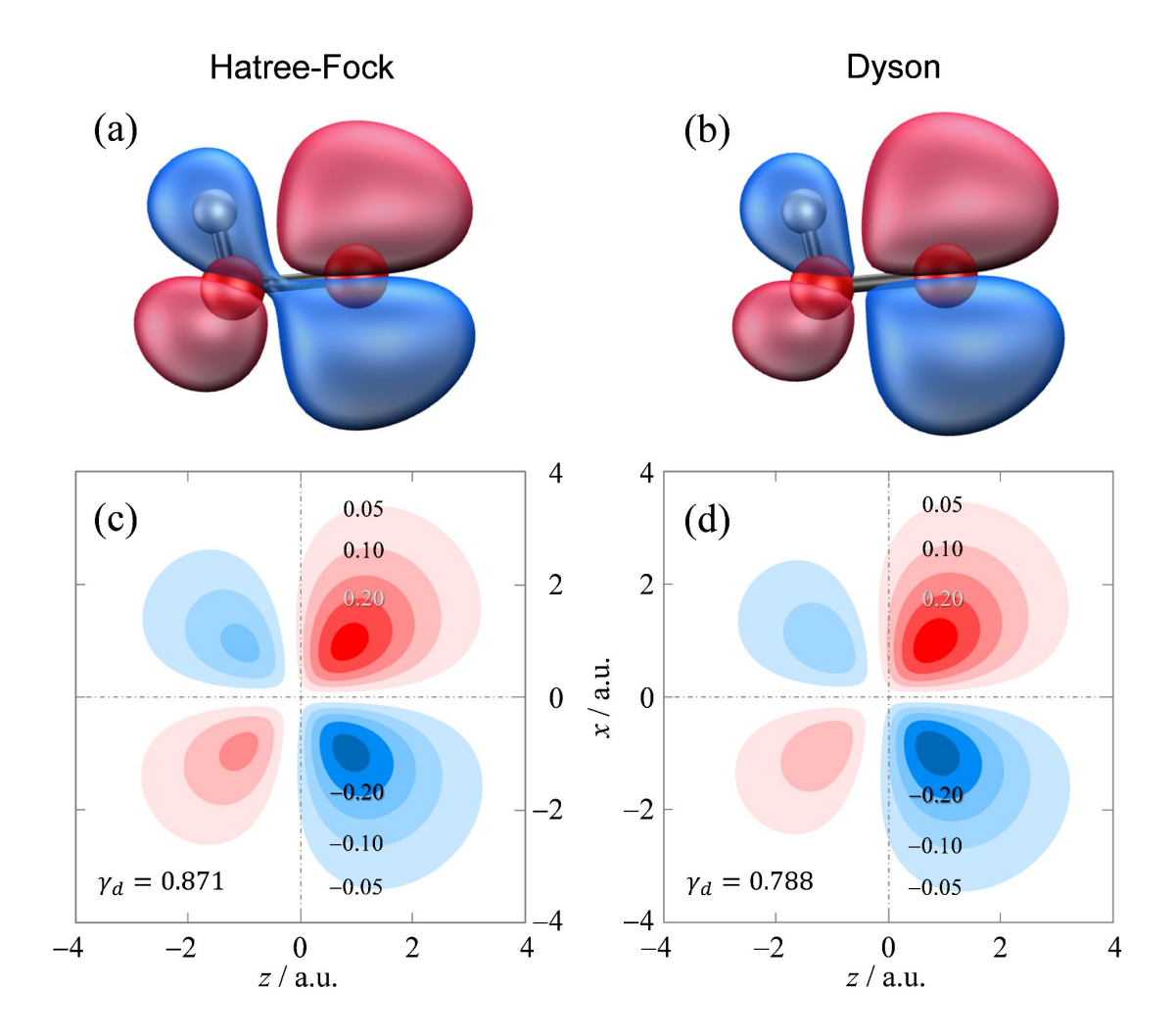


Figure 5. (a) Canonical HF and (b) Dyson orbitals, corresponding to photodetachment from the a' HOMO–1 of HO₂⁻. (c)-(d) Cross-sections of the model functions defined by equation (1), representing the above orbitals.

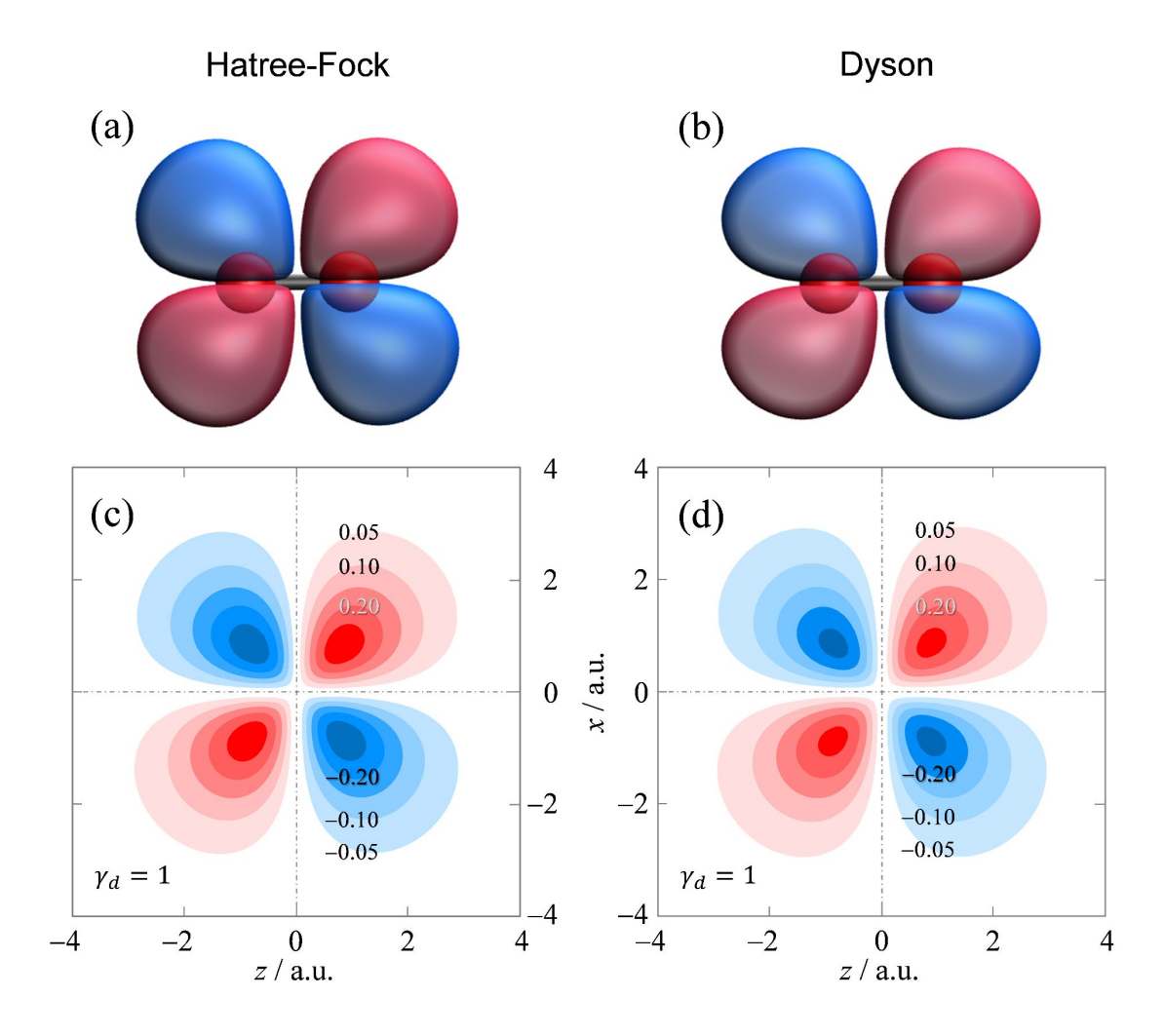


Figure 6. (a) Canonical HF and (b) Dyson orbitals, corresponding to photodetachment from the π_g^* HOMO of O_2^- . (c)-(d) Cross-sections of the model functions defined by equation (1), representing the above orbitals. In this case, for both HF and Dyson orbitals, γ_d is strictly equal to 1, by symmetry.

Figure 7

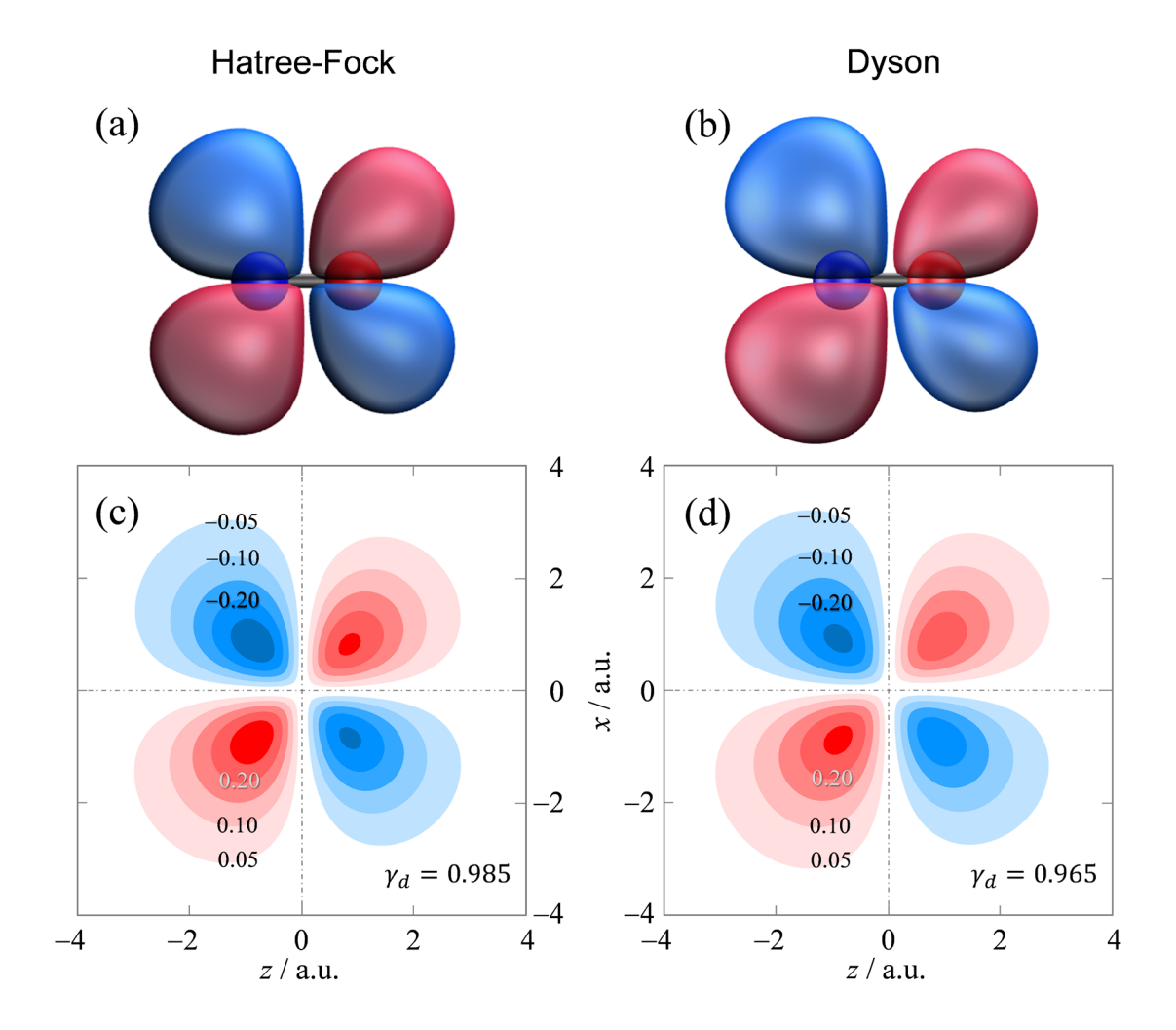


Figure 7. (a) Canonical HF and (b) Dyson orbitals, corresponding to photodetachment from the HOMO of NO⁻. (c)-(d) Cross-sections of the model functions defined by equation (1), representing the above orbitals.

Figure 8

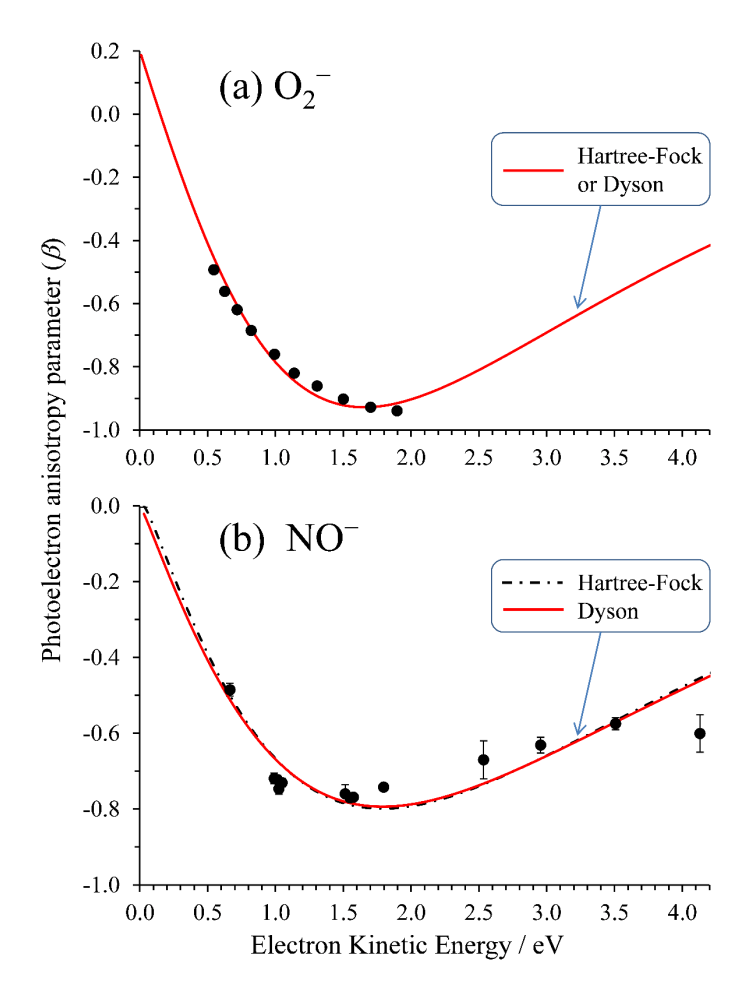


Figure 8. Symbols show measured anisotropy parameter β , plotted as a function of electron kinetic energy, for the (a) $O_2(X^3\Sigma_g^-, v'=2) \leftarrow O_2^-(X^2\Pi_g, v''=0)$ and (b) $NO(X^2\Pi, v'=2) \leftarrow NO^-(X^3\Sigma^-, v''=0)$ vertical photodetachment transitions. Data sources are cited in the text. Solid curves represent fits to the experimental data using p-d model equation (3). In (a), the γ_d value was constrained to strictly 1 (by symmetry); hence both the HF and Dyson orbitals yield indistinguishable model curves. In (b), the γ_d value was constrained to $\gamma_d = 0.985$ for the Hartree-Fock HOMO (dash-dotted black curve) and to $\gamma_d = 0.965$ for the Dyson orbital (solid red curve). The resulting ζ_{2p} and ζ_{3d} values are given in the PAD data fits part of Table 1.